



JGR Solid Earth



RESEARCH ARTICLE

10.1029/2019JB018447

Key Points:

- We studied phase relations in the system $\text{MgSiO}_3\text{-FeAlO}_3$ at 27 GPa and 2000 K
- We determined the stability, solubility, and thermoelastic properties of the FeAlO_3 component in bridgmanite
- We applied this knowledge of the FeAlO_3 component to obtain new insight into the mineralogy of the lower mantle

Correspondence to:

Z. Liu,
liu_zhaodong@jlu.edu.cn

Citation:

Liu, Z., McCammon, C., Wang, B., Dubrovinsky, L., Ishii, T., Bondar, D., et al. (2020). Stability and solubility of the FeAlO_3 component in bridgmanite at uppermost lower mantle conditions. *Journal of Geophysical Research: Solid Earth*, 125, e2019JB018447. <https://doi.org/10.1029/2019JB018447>

Received 30 JUL 2019

Accepted 5 FEB 2020

Accepted article online 7 FEB 2020

Stability and Solubility of the FeAlO_3 Component in Bridgmanite at Uppermost Lower Mantle Conditions

Zhaodong Liu^{1,2} , Catherine McCammon¹ , Biao Wang¹, Leonid Dubrovinsky¹, Takayuki Ishii¹ , Dmitry Bondar¹, Ayano Nakajima³, Yoshinori Tange⁴ , Yuji Higo⁴ , Tian Cui², Bingbing Liu², and Tomoo Katsura^{1,5}

¹Bayerisches Geoinstitut, University of Bayreuth, Bayreuth, Germany, ²State Key Laboratory of Superhard Materials, Jilin University, Changchun, China, ³Department of Earth Sciences, Graduate School of Science, Tohoku University, Sendai, Japan, ⁴SPring-8, Japan Synchrotron Radiation Institute, Hyogo, Japan, ⁵Center for High Pressure Science and Technology Advanced Research, Beijing, China

Abstract We report the stability and solubility of the FeAlO_3 component in bridgmanite based on phase relations in the system $\text{MgSiO}_3\text{-FeAlO}_3$ at 27 GPa and 2000 K using a multi-anvil apparatus combined with in situ synchrotron X-ray diffraction measurements. The results demonstrate that the FeAlO_3 component dominates Fe^{3+} and Al^{3+} substitution in bridgmanite, although trace amounts of oxygen- and Mg-site vacancy components are also present. Bridgmanite with more than 40 mol% FeAlO_3 transforms into the LiNbO_3 -type phase upon decompression. The FeAlO_3 end-member decomposes into corundum and hematite and does not form single-phase bridgmanite. We determined the maximum solubility of the FeAlO_3 component in bridgmanite at 27 GPa and 2000 K to be 67 mol%, which is significantly higher than previously reported values (25–36 mol%). We determined the partial molar volume (27.9 mol/cm³) and bulk modulus (197 GPa) of hypothetical FeAlO_3 bridgmanite, which are significantly higher and lower than those of AlAlO_3 and FeSiO_3 bridgmanite, respectively. The non-ideality of $\text{MgSiO}_3\text{-FeAlO}_3$ solid solution ($W = 13 \text{ kJ/mol}$, where W is the interaction parameter) is significantly larger than that for $\text{MgSiO}_3\text{-AlAlO}_3$ (5 kJ/mol) and $\text{MgSiO}_3\text{-FeSiO}_3$ (3 kJ/mol) solid solutions. The rapid decrease in abundance of the $\text{MgAlO}_{2.5}$ component in bridgmanite with increasing pressure is enhanced by the presence of the FeAlO_3 component. The FeAlO_3 content in pyrolite and mid-ocean ridge basalt is far below its solubility limit in bridgmanite and provides new insight into the mineralogy of the lower mantle.

1. Introduction

Bridgmanite is not a pure MgSiO_3 phase in Earth's lower mantle but contains a significant amount of other elements such as aluminum (Al) and iron (Fe) (Irifune, 1994; McCammon, 1997). Although the oxidation state in the lower mantle is considered very reduced, Fe preferably forms the charge-coupled $\text{Fe}^{3+}\text{AlO}_3$ component in bridgmanite in addition to the $\text{Fe}^{2+}\text{SiO}_3$ component in the presence of Al (Frost et al., 2004; Frost & Langenhorst, 2002; McCammon, 1997). The FeAlO_3 component is one of the dominant trivalent components in bridgmanite (Frost & Langenhorst, 2002; Richmond & Brodholt, 1998). The incorporation of FeAlO_3 can significantly affect physical and chemical properties of bridgmanite such as elasticity (e.g., Andrault et al., 2007; Boffa Ballaran et al., 2012), electrical conductivity (e.g., Xu et al., 1998; Yoshino et al., 2016), spin-transition pressure of Fe (e.g., Badro et al., 2004; Fujino et al., 2012), and Mg-Fe partitioning (Frost & Langenhorst, 2002). The component can thus influence seismic wave velocities (Glazyrin et al., 2014) and viscosity (Shim et al., 2017) in the lower mantle. In particular, Kurnosov et al. (2017) reported that FeAlO_3 -dominated bridgmanite shows lower bulk and shear moduli than the MgSiO_3 component. Therefore, studies of the chemical and physical behavior of the FeAlO_3 component in bridgmanite are important for understanding the structure and dynamics of Earth's lower mantle.

In spite of its significance, our knowledge of the chemical-physical behavior of the FeAlO_3 component in bridgmanite is limited. Ab initio simulations by Richmond and Brodholt (1998) suggested that the charge-coupled FeAlO_3 component is energetically favored for Fe^{3+} and Al^{3+} substitution in bridgmanite throughout the lower mantle. Petrological experiments showed that the FeAlO_3 content in bridgmanite increases with increasing trivalent cation content (Frost & Langenhorst, 2002; Lauterbach et al., 2000) and pressure

©2020. The Authors.

This is an open access article under the terms of the Creative Commons Attribution License, which permits use, distribution and reproduction in any medium, provided the original work is properly cited.

(Andrault et al., 2018). Furthermore, the end-member FeAlO_3 was found to possess a $\text{Rh}_2\text{O}_3(\text{II})$ structure rather than the perovskite structure at lower mantle conditions (Nagai et al., 2005); hence, there is a solubility limit for FeAlO_3 in bridgmanite as a function of pressure and temperature. Indeed, Nishio-Hamane et al. (2005) reported that the abundance of the FeAlO_3 component in bridgmanite was slightly lower and higher than 25 mol% at 24 and 51 GPa, respectively, at 2100 K based on laser-heated diamond anvil cell experiments. Their study was only qualitative, however, and could not provide quantitative data regarding FeAlO_3 component solubility because Fe oxidation state was not measured. Subsequently, Boffa Ballaran et al. (2012) reported that bridgmanite can contain up to 36 mol% FeAlO_3 component based on synthesis from a hydrous oxide mixture at 25 GPa and 1600 K using a multi-anvil press but did not investigate the maximum solubility limit. The question of the stability and solubility of the FeAlO_3 component in bridgmanite thus still remains open. We further emphasize that determination of the maximum solubility of the FeAlO_3 component requires synthesis of bridgmanite coexisting with excess FeAlO_3^- , $\text{FeO}_{1.5}^-$, or $\text{AlO}_{1.5}$ -rich phase, which has not been achieved in previous experiments.

Here, we investigate the stability and solubility of the FeAlO_3 component in bridgmanite by studying phase relations in the system MgSiO_3 - FeAlO_3 at 27 GPa and 2000 K using a multi-anvil apparatus. We determine the phase stability of bridgmanite and LiNbO_3 -type phase as a function of FeAlO_3 content and the maximum solubility of the FeAlO_3 component in bridgmanite. Finally, we discuss the chemistry and thermoelastic properties of bridgmanite and implications for the mineralogy and dynamics of the lower mantle.

2. Materials and Methods

2.1. Starting Material Preparation

The main starting materials were glass powders with FeAlO_3 contents of $\text{En}_x\text{FA}_{100-x}$, where $x = 90, 75$, and 60 (x means mol%; En: MgSiO_3 , FA: $\text{Fe}^{3+}\text{AlO}_3$), and fine-grained oxide mixtures with FeAlO_3 contents of $\text{En}_{50}\text{FA}_{50}$ and $\text{En}_{25}\text{FA}_{75}$ ($^{57}\text{Fe}_2\text{O}_3$ was used in some samples to facilitate determination of the $\text{Fe}^{3+}/\Sigma\text{Fe}$ ratio of run products). A mixture of 90 mol% $\text{En}_{25}\text{FA}_{75}$ fine-grained oxide mixtures and 10 mol% $^{57}\text{Fe}_2\text{O}_3$ hematite was prepared to ensure excess Fe^{3+} . In addition to these mixtures with the MgSiO_3 component, we also prepared an FeAlO_3 (FA_{100}) compound with the FeGaO_3 -type structure.

Glasses were prepared from mixtures of reagent-grade chemicals of MgO , SiO_2 , Fe_2O_3 , and Al_2O_3 that were fused at 2000 K for 30 min and quenched into water. This process was repeated three times to ensure homogeneity of the glasses. Fine-grained oxide mixtures were prepared by mechanically mixing reagent-grade oxide chemicals (grain sizes below 1 μm , which were sufficient to ensure reaction at 27 GPa and 2000 K) with ethanol for 3 hr. FeGaO_3 -structured FeAlO_3 was synthesized by heating a fine-grained mixture of Fe_2O_3 and Al_2O_3 with molar ratio 1:1 at 1670 K in air for 15 hr.

2.2. High-Pressure and High-Temperature Experiments

Starting materials were loaded into platinum capsules and heated to 800 K for 1 hr before placing into high-pressure cell assemblies to avoid reduction of Fe_2O_3 and minimize adsorbed water. We used Cr_2O_3 -doped MgO octahedra with 7-mm edge length and LaCrO_3 sleeves for heating (Liu et al., 2019) in combination with tungsten carbide cubes with 3-mm truncated edge length. Experiments were performed in a Kawai-type multi-anvil apparatus (IRIS-15) with a maximum press load of 15 MN at the Bayerisches Geoinstitut, University of Bayreuth (Ishii et al., 2016). Experiments were quenched after heating at 27 GPa and 2000 K for 6 to 24 hr (Table 1).

2.3. Analytical Methods

Phases in recovered samples were identified using a micro-focus X-ray diffractometer with a Co anode operated at 40 kV and 500 mA. MgSiO_3 bridgmanite was used as an external standard to calibrate the Bragg angle (2θ) of the diffractometer. X-ray diffraction (XRD) profiles were collected for 3 hr for each sample. Backscattered electron (BSE) images of $\text{En}_{90}\text{FA}_{10}$ and $\text{En}_{75}\text{FA}_{25}$ samples were obtained using a LEO1530 scanning electron microscope operating at an acceleration voltage of 15 kV. Phase compositions and BSE images of other samples were determined by a JEOL JXA-8200 electron probe microanalyzer operating at an acceleration voltage of 15 kV and a beam current of 5–10 nA with standards of enstatite for Mg and Si, corundum for Al, and iron metal for Fe.

Table 1
Details of Experimental Runs at 27 GPa and 2000 K

Run No.	Starting composition	Heating time (hr)	Phases
IRIS483	En ₉₀ FA ₁₀	6	Brg
IRIS428	En ₇₅ FA ₂₅	20	Brg
IRIS517	En ₆₀ FA ₄₀	20	Brg/LN
IRIS427 ^a	En ₅₀ FA ₅₀	24	LN
IRIS461	En ₂₅ FA ₇₅	26	LN + Cor + trace Hem
	FA ₁₀₀		Cor + Hem + trace Ox
IRIS493	En ₂₅ FA ₇₅ + ⁵⁷ Fe ₂ O ₃	24	LN + Cor + Hem

Abbreviations: Brg = bridgmanite; Cor = corundum; Hem = hematite; LN = LiNbO₃-type phase; Ox = iron oxide (Fe₄O₅).

^aReported in Liu, Dubrovinsky, et al. (2019).

We selected crystals of dominant phases (bridgmanite and LiNbO₃-type phase) in run products for determination of Fe³⁺/ΣFe ratios using Mössbauer spectroscopy, which was conducted in transmission mode on a constant acceleration Mössbauer spectrometer with a nominal 370-MBq ⁵⁷Co point source in a 12-μm Rh matrix. The velocity scale was calibrated relative to α-Fe. The dimensionless Mössbauer thickness of each sample varied from 4 to 50, and spectra were collected for between 10 hr and 5 days each. Spectra were fit with MossA software using doublets with pseudo-Voigt lineshapes and the full transmission integral (Prescher et al., 2012). Fe³⁺/ΣFe ratios were determined from relative areas. Further information about the Mössbauer setup can be found in McCammon (1994).

2.4. In Situ X-ray Diffraction Experiments

A run product from the En₅₀Cor₅₀ starting material was found to have the LiNbO₃-type structure instead of the perovskite structure; so in order to investigate its stability, in situ XRD experiments were performed at 28 GPa and 2000 K using tungsten carbide anvils with truncated edge length of 3 mm as second-stage anvils in a DIA-type multi-anvil apparatus at the synchrotron radiation facility, SPring-8 (SPEED-Mk. II). The experimental facility for in situ XRD measurements was described by Katsura et al. (2004), and the in situ high-pressure cell assembly was almost identical to that of the synthesis experiment except that the former has two open circles as X-ray windows in the middle position of the LaCrO₃ heater. Au powder was placed between the sample, and MgO powder was placed on top of the hot junction of the thermocouple. Pressures were determined based on the P-V-T equation of state of Au proposed by Tsuchiya (2003). Uncertainties in pressure determination in these in situ experiments are approximately ±0.2 GPa. Sample temperatures were measured with a W₉₇Re₃-W₇₅Re₂₅ thermocouple, whose hot junction was placed in the middle position of the LaCrO₃ heater. The sample was compressed to the target pressure and then heated at the target temperature for 1 hr. In situ XRD patterns were collected for 1 hr at the target pressure and temperature. Then, the run was quenched by turning off the electric power, and the pressure was released slowly over several hours.

3. Results

3.1. Phase Identification by XRD Patterns and BSE Images of Quench Experiments

Table 1 lists the starting materials, experimental conditions, and run products. Figures 1 and 2, respectively, show all XRD patterns and BSE images of recovered samples. All XRD peaks of the recovered samples for the En₉₀FA₁₀ and En₇₅FA₂₅ samples can be assigned to bridgmanite. BSE images further confirm that there is only a single phase of bridgmanite with grain size of 2–10 μm. In contrast, sample En₆₀FA₄₀ shows several strong diffraction peaks that can be assigned to the LiNbO₃ (LN)-type phase (Megaw, 1968) in addition to peaks of bridgmanite (Figure 1c). The BSE image shows no distinguishable BSE signal intensities between bridgmanite and the LN-type phase, indicating nearly identical compositions of these two phases. The BSE image (Figure 2c) demonstrates that the grain size of this sample is relatively large, approximately 100 μm. The XRD pattern of sample En₅₀FA₅₀ (Figure 1d) shows only the LN-type phase. Its BSE image (Figure 2d) shows a uniform phase composition and a large grain size of 200–300 μm, which is even larger than the grain size of sample En₆₀FA₄₀ (Figure 2c).

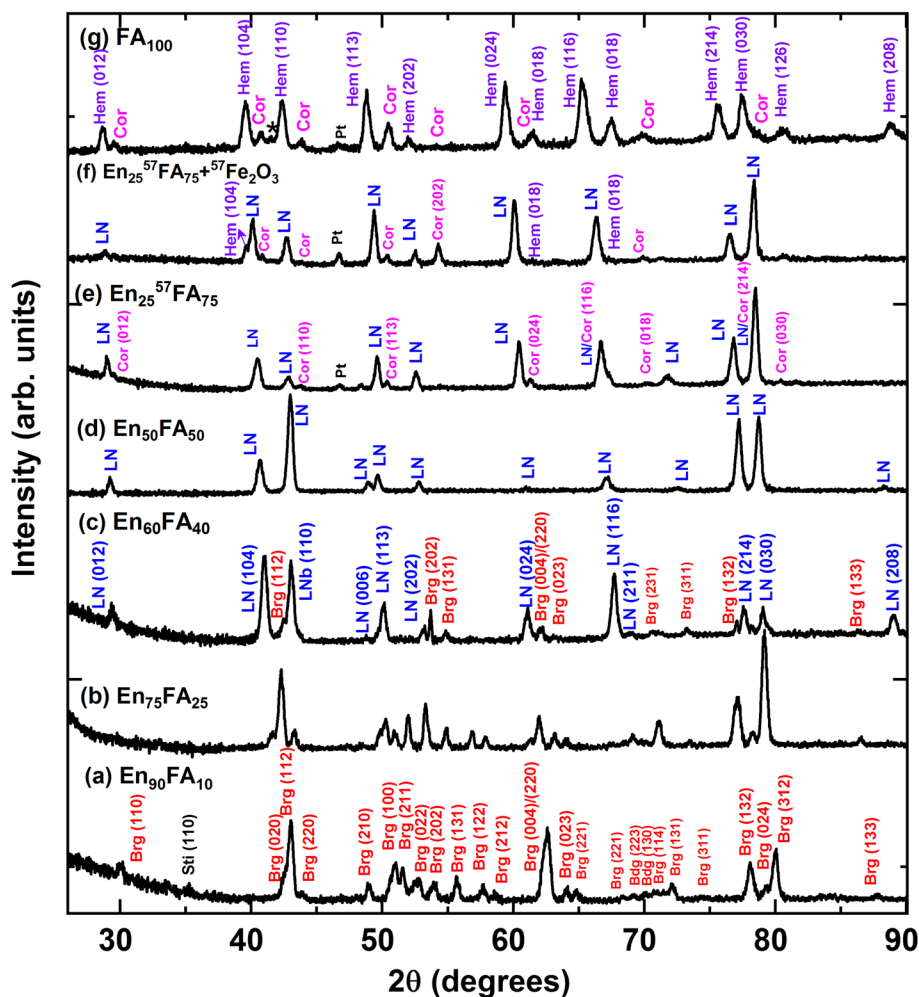


Figure 1. XRD profiles of En_xFA_{100 - x} ($x = 90, 75, 60, 50, 25$, and 0 mol%) in the system MgSiO₃ (En)-FeAlO₃ (FA). Asterisks represent peaks from the iron oxide phase (Fe₄O₅). Brg = bridgemanite; Cor = corundum; Hem = hematite; LN = LiNbO₃-type phase; Sti = stishovite.

XRD patterns of the En₂₅FA₇₅ composition without additional ⁵⁷Fe₂O₃ show the LN-type phase plus corundum (Figure 1e). The BSE image shows a trace amount of an Fe₂O₃ phase (hematite) in this sample (Figure 2e). The XRD pattern of En₂₅FA₇₅ with excess ⁵⁷Fe₂O₃ shows strong peaks of hematite as expected (Figure 1f) in addition to the LN-type phase and corundum, which appears in the sample without additional ⁵⁷Fe₂O₃ (Figure 1e). The BSE image of this sample (Figure 2f) combined with the XRD pattern suggests the coexistence of the LN-type phase, hematite, and corundum. The XRD pattern (Figure 1g) and BSE image (Figure 2g) of the FeAlO₃ sample show the coexistence of corundum, hematite, and trace amounts of an iron oxide phase. The XRD pattern suggests that the iron oxide phase may be Fe₄O₅. Neither bridgemanite nor the LN-type phase was observed in this sample.

3.2. Fe³⁺/ΣFe Ratios by Mössbauer Spectroscopy

Figure 3 shows Mössbauer spectra of bridgemanite and LN-type phase from four samples. Hyperfine parameters (Table 2) are consistent with those reported by McCammon et al. (2004) for bridgemanite. In other words, hyperfine parameters are highly similar for bridgemanite and the LN-type phase. The Fe³⁺/ΣFe ratios were found to be 85–90 mol% within analytical uncertainty except for the En₉₀FA₁₀ sample, which may be smaller (76%), although its analytical error is large (15%). The Fe³⁺/ΣFe ratio of the En₅₀FA₅₀ sample is close to 100% within uncertainty according to our recent study (Liu, Dubrovinsky, et al., 2019).

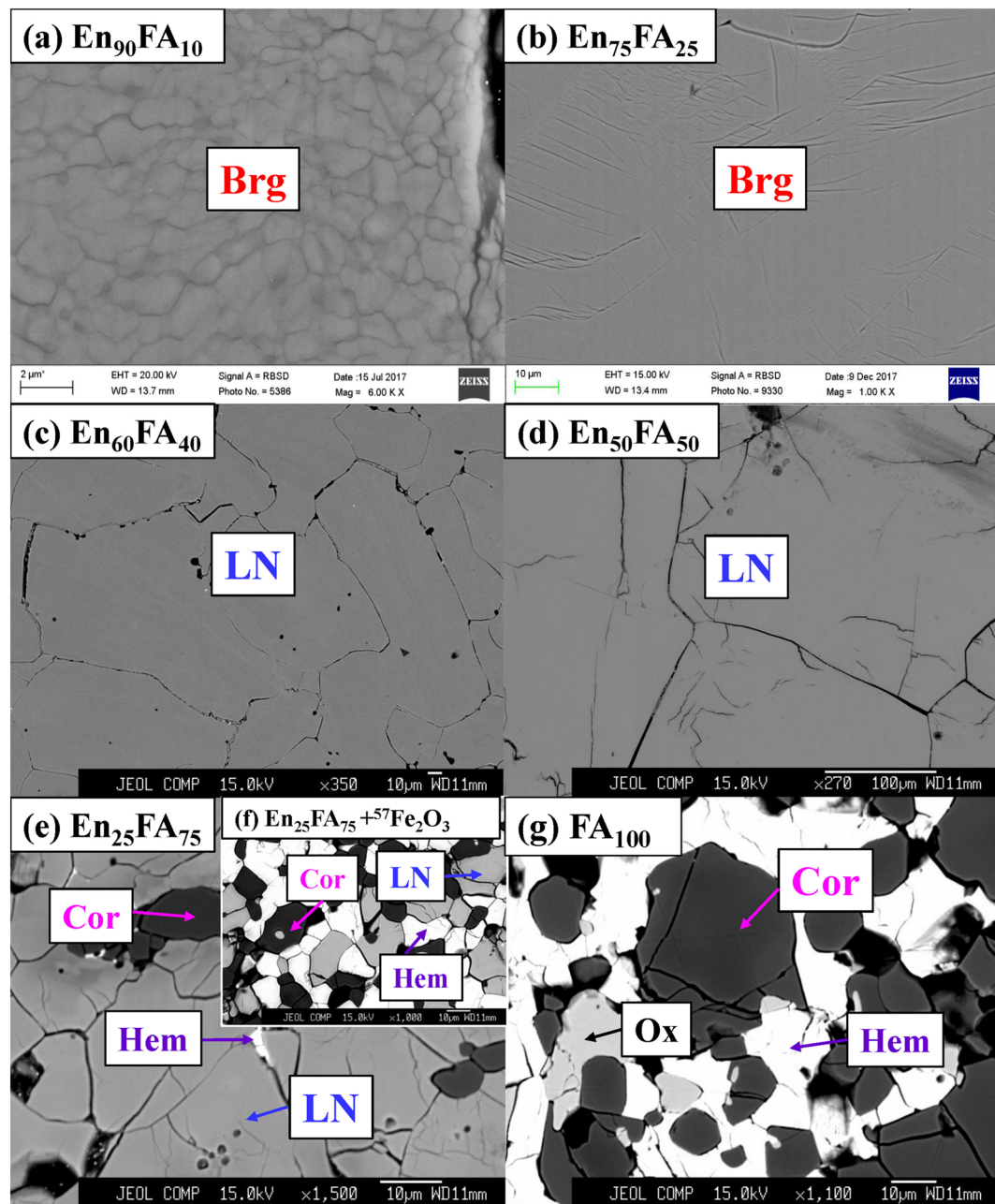


Figure 2. BSE images of run products of the $\text{En}_x\text{FA}_{100-x}$ sample ($x = 90, 75, 60, 50, 25$, and $0 \text{ mol}\%$). Brg = bridgmanite; Cor = corundum; Hem = hematite; LN = LiNbO_3 -type phase; O_x = iron oxide phase.

3.3. Phase Transition Observed by In Situ XRD

We conducted in situ XRD on one pre-synthesized LN -type $(\text{Mg}_{0.5}\text{Fe}^{3+}_{0.5})(\text{Si}_{0.5}\text{Al}^{3+}_{0.5})\text{O}_3$ phase up to 28 GPa and 2000 K. As shown in Figure 4a, the peaks can be assigned to those of LN -type phase with some MgO peaks from surrounding cell parts at ambient conditions. The sample was compressed to 13 MN (33 GPa), which is the same press load used for in-house synthesis experiments; at this pressure, the material already transformed into bridgmanite according to XRD observations (Figure 4a). We increased temperature to 2000 K, then reduced pressure to 28 GPa, and the sample remained in the perovskite structure with lattice parameters of $a = 4.697$ (2) Å, $b = 4.883$ (1) Å, $c = 6.813$ (2) Å, and $V = 156.3$ (2) Å³. After decompression, we collected a micro-XRD pattern of the recovered sample and found that it had reverted to the LN -type

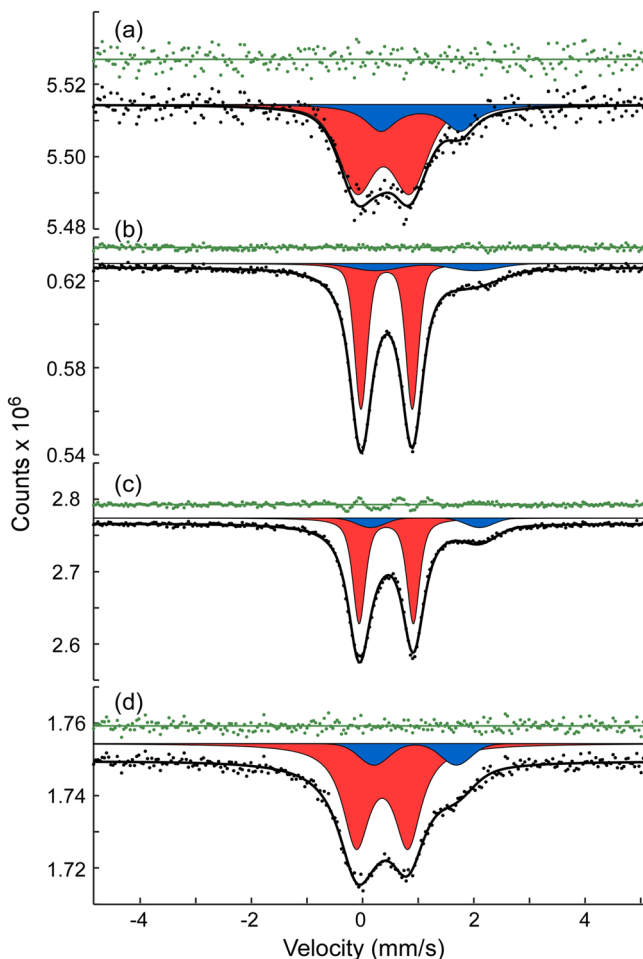


Figure 3. Room temperature Mössbauer spectra of bridgmanite and the *LN*-type phase: (a) En₉₀FA₁₀, (b) En₇₅FA₂₅, (c) En₆₀FA₄₀, and (d) En₂₅FA₇₅. Absorption assigned to Fe²⁺ and Fe³⁺ is shaded blue and red, respectively, and the fit residual is shown in green above each spectrum.

40 mol% FeAlO₃. Ishii et al. (2017) argued that the transition from bridgmanite to the *LN*-type phase occurs because the ionic radii of cations in the A site are too small to preserve the perovskite structure during decompression. The ionic radii of Mg²⁺ and Al³⁺ in sixfold coordination (ionic radii in 12-fold coordination are unavailable) are 0.72 and 0.535 Å, respectively (Shannon, 1976). On the other hand, the ionic radius of high-spin Fe³⁺ in sixfold coordination is 0.645 Å (Shannon, 1976), which is between those of Mg²⁺ and Al³⁺. This can explain why the FeAlO₃ component requires a higher abundance for the bridgmanite to the *LN*-type phase transition compared to the Al₂O₃ component. In addition, the closer similarity of ionic radii between Mg²⁺ and Fe³⁺ compared to Mg²⁺ and Al³⁺ allows less pressure for accommodation of the FeAlO₃ component than for Al₂O₃, which can explain the lower pressure required for the transition from bridgmanite to the *LN*-type phase.

4.2. Fraction of Trivalent and Divalent Components in Bridgmanite

Bridgmanite/*LN*-type phase contains more components than MgSiO₃ and FeAlO₃, since some Fe³⁺ was reduced to Fe²⁺ and the amount of Al was not equal to that of Fe. However, the species and their proportions in bridgmanite/*LN*-type phase cannot be uniquely determined because of these potential additional components. Therefore, we calculated fractions of trivalent and divalent components according to the following assumptions. Firstly, the divalent cations Mg²⁺ and Fe²⁺ will be accommodated in the A site, whereas the tetravalent cation Si⁴⁺ will be accommodated in the B site. Secondly, the majority of Fe³⁺ cations will be accommodated in the A (Mg²⁺) site, while the majority of Al³⁺ cations will be accommodated in the B

phase again (Figure 4b). In situ XRD observations clearly demonstrate that the FeAlO₃-rich *LN*-type phase is formed by back-transformation from bridgmanite upon decompression.

4. Discussion

4.1. Phase Transition of Bridgmanite to the *LN*-Type Phase Upon Decompression

Bridgmanite was observed in XRD and BSE data of run products for starting compositions with relatively low FeAlO₃ contents (En₉₀FA₁₀, En₇₅FA₂₅, and En₆₀FA₄₀), whereas the *LN*-type phase was observed in those with higher FeAlO₃ contents (En₆₀FA₄₀, En₅₀FA₅₀, and En₂₅FA₇₅). These two phases coexisted in the same En₆₀FA₄₀ sample. One possible explanation for the presence of these two phases is that they are both stable at different bulk compositions. If this is the case, these phases form a binary phase loop, in which a compositional gap should exist between the two phases. Nevertheless, the compositions of coexisting bridgmanite and *LN*-type phase are highly similar as mentioned previously. Hence, we infer that one of these phases must be metastable.

Previous studies demonstrated that Al₂O₃-rich bridgmanite transforms to the *LN*-type phase upon decompression at ambient temperature (Funamori et al., 1997; Ishii et al., 2017; Liu et al., 2016; Liu, Ishii, & Katsura, 2017; Liu, Dubrovinsky, et al., 2019; Miyajima et al., 1999). In situ XRD observations (Figure 4) demonstrate that the same phase transition occurs in the En₅₀FA₅₀ sample. The crystal structure of En₅₀FA₅₀ *LN*-type phase has been described by Liu, Dubrovinsky, et al. (2019). The coexistence of bridgmanite and *LN*-type phase in the sample En₆₀FA₄₀ can thus be explained by an incomplete phase transition from bridgmanite to the *LN*-type phase upon decompression.

Early studies found that bridgmanite with pyrope composition, namely, 25 mol% of Al₂O₃ component, transformed into the *LN*-type phase upon quenching from 45 GPa at 2000 K (Ishii et al., 2017; Liu et al., 2016; Liu, Nishi, et al., 2017). The present study demonstrates that this transition occurs at a lower pressure of 27 GPa but with a secondary component of

Table 2Compositions, Cation Components, and Hyperfine Parameters of Bridgmanite/LiNbO₃-Type Phase

	Run. No.					
	IRIS483	IRIS428	IRIS517	IRIS427 ^a	IRIS461	IRIS493
	Composition					
	En ₉₀ FA ₁₀	En ₇₅ FA ₂₅	En ₆₀ FA ₄₀	En ₅₀ FA ₅₀	En ₂₅ FA ₇₅	En ₂₅ FA ₇₅ + ⁵⁷ Fe ₂ O ₃
MgO	Brg (<i>n</i> = 10) 34.74 (36)	Brg (<i>n</i> = 30) 29.11 (46)	Brg/LN (<i>n</i> = 10) 20.63 (36)	LN (<i>n</i> = 15) 16.95 (57)	LN (<i>n</i> = 25) 7.79 (47)	LN (<i>n</i> = 35) 7.61 (47)
Al ₂ O ₃	5.35 (42)	12.02 (35)	19.14 (23)	22.90 (28)	28.96 (46)	25.74 (78)
FeO	5.25 (25)	11.38 (63)	23.81 (32)	30.73 (50)	45.55 (76)	47.58 (92)
SiO ₂	54.06 (44)	46.06 (39)	34.24 (54)	25.97 (61)	13.15 (68)	15.41 (82)
Total	99.40 (48)	98.55 (81)	97.82 (58)	96.54 (88)	95.75 (74)	96.34 (60)
Fe ³⁺ ΣFe	76 (15)	87 (4)	87 (4)	100	89 (5)	85 (8)
Mg	0.881 (13)	0.768 (9)	0.574 (10)	0.487 (11)	0.244 (14)	0.236 (14)
Al	0.107 (8)	0.251 (7)	0.421 (6)	0.517 (10)	0.718 (13)	0.630 (20)
Fe ³⁺	0.056 (9)	0.144 (9)	0.320 (12)	0.493 (9)	0.671 (10)	0.692 (16)
Fe ²⁺	0.037 (20)	0.022 (6)	0.046 (11)		0.118 (10)	0.123 (13)
Si	0.919 (12)	0.815 (8)	0.639 (8)	0.502 (9)	0.277 (12)	0.320 (16)
O	3.001 (12)	3.013 (7)	3.010 (9)	3.008 (5)	2.029 (5)	2.981 (6)
Component (mol%)						
MgSiO ₃	88 (1)	77 (1)	57 (1)	49 (1)	20 (1)	20 (2)
FeSiO ₃	4 (2)	2 (1)	5 (1)	0	9 (3)	12 (0)
FeAlO ₃	6 (1)	11 (1)	29 (2)	49 (1)	65 (4)	63 (2)
AlAlO ₃	2 (2)	7 (1)	7 (1)	1 (1)	N	N
FeFeO ₃	N	N	N	N	0	1 (1)
MgAlO _{2.5}	N	N	N	N	6 (3)	N
MgFeO _{2.5}	N	N	N	N	N	4 (1)
Al _{2/3} SiO ₃	N	N	N	1 (1)	N	N
Fe _{2/3} SiO ₃	N	3 (2)	2 (2)	N	N	N
Total	100	100	100	100	100	100
Hyperfine parameters						
CS Fe ²⁺	1.04 (9)	1.13 (4)	1.12 (3)	N	1.01 (fixed)	0.94 (6)
QS Fe ²⁺	1.43 (13)	1.78 (6)	1.96 (7)	N	1.55 (fixed)	1.48 (9)
FWHM Fe ²⁺	0.67 (32)	1.01 (13)	0.59 (12)	N	1.10 (fixed)	0.63 (20)
CS Fe ³⁺	0.37 (3)	0.43 (1)	0.43 (1)	0.34 (1)	0.35 (1) ^b	0.35 (2)
QS Fe ³⁺	0.94 (6)	0.92 (1)	0.98 (1)	0.91 (1)	0.88 (1)	0.93 (3)
FWHM Fe ³⁺	0.77 (7)	0.27 (1)	0.27 (1)	0.18 (2)	0.53 (2)	0.59 (6)

Abbreviations: Bdg = bridgmanite; CS = center shift relative to α-Fe (mm/s); FWHM = full width at half maximum (mm/s); LN = LiNbO₃-type phase; *n* = number of analysis points; N = not present; QS = quadrupole splitting (mm/s).

^aReported in Liu, Dubrovinsky, et al. (2019). ^bBroad magnetic Fe³⁺ component also present with CS = 0.25 mm/s, BHF (magnetic hyperfine field) = 8.3 (28) T, and FWHM = 3.5 (3) mm/s.

(Si⁴⁺) site based on the similar effective ionic radii of Fe³⁺ (0.645 Å) and Mg²⁺ (0.72 Å) and those of Al³⁺ (0.535 Å) and Si⁴⁺ (0.40 Å; Shannon, 1976). This assumption is valid at least in the uppermost part of the lower mantle (Fujino et al., 2012). If the number of Fe³⁺ or Al³⁺ cations is too large for the A or B site, the rest of Fe³⁺ or Al³⁺ will be accommodated in the B or A site, respectively. Thirdly, oxygen- and A-site cation vacancies will form if the cation/anion ratio is larger or smaller, respectively, than two thirds (Ismailova et al., 2016). Namely, if the cation number difference *d* = (Si-Mg-Fe²⁺) is positive, an A-site vacancy will form as a Fe_{2/3}SiO₃ component. If the value of *d* is negative, the oxygen vacancy component MgAlO_{2.5} will form. Fourthly, the remaining Fe³⁺ and Al³⁺ will firstly form FeAlO₃, and then either FeFeO₃ or AlAlO₃ components if the amount of the remaining Fe³⁺ or Al³⁺ is not equal.

The results of our calculations are shown in Table 2. The trivalent and divalent components considered are MgSiO₃, FeSiO₃, FeAlO₃, MgAlO_{2.5}, MgFeO_{2.5}, AlAlO₃, FeFeO₃, and Fe_{2/3}SiO₃. The most important conclusion is that the maximum FeAlO₃ content reaches 65 mol% at our experimental conditions of 27 GPa and 2000 K. Bridgmanite thus accommodates a large amount of the FeAlO₃ component. Other important features are as follows: (1) At very low FeAlO₃ contents (En₉₀FA₁₀), bridgmanite is nearly stoichiometric; (2) at slightly higher FeAlO₃ contents (En₇₅FA₂₅ and En₆₀FA₄₀), the A-site vacancy component Al_{2/3}SiO₃

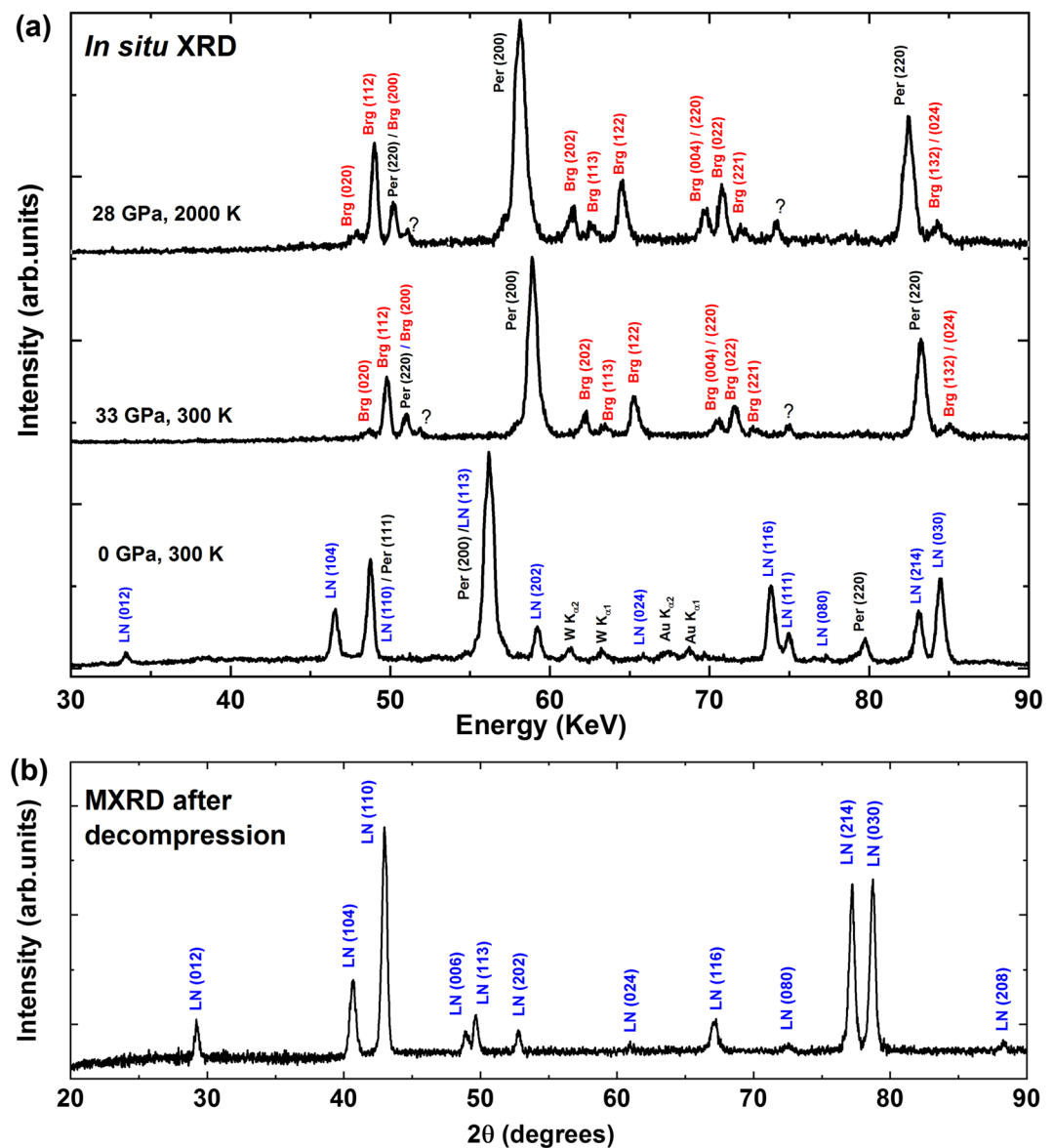


Figure 4. (a) In situ energy-dispersive XRD patterns of synthetic $\text{En}_{50}\text{FA}_{50}$ LN -type phase at different conditions. (b) MXRD of the recovered sample shown in (a). Brg = bridgmanite; LN = LiNbO_3 -type phase; Per = periclase from surrounding MgO sleeves.

appears; (3) at even higher FeAlO_3 contents ($\text{En}_{50}\text{FA}_{50}$ and $\text{En}_{25}\text{FA}_{75}$), no A-site vacancy but rather oxygen vacancy components appear; (4) at the highest Fe_2O_3 composition, Fe^{3+} enters the B site to form the oxygen vacancy component $\text{MgFeO}_{2.5}$ and the charge-coupled FeFeO_3 component. If we consider that all Fe is Fe^{3+} as in the case of the $\text{En}_{50}\text{FA}_{50}$ sample, the maximum FeAlO_3 content in bridgmanite would be even higher than the present result because of the charge-coupled substitution of Fe^{3+} and Al^{3+} in oxidized environments.

4.3. Solubility of the FeAlO_3 Component in Bridgmanite

As shown in Table 2, the FeAlO_3 component in bridgmanite/ LN -type phase monotonically increases from 6 to 49 mol% with increasing FeAlO_3 component in the bulk starting composition from $\text{En}_{90}\text{FA}_{10}$ to $\text{En}_{50}\text{FA}_{50}$. The maximum FeAlO_3 content of 65 mol% was obtained from the starting material of $\text{En}_{25}\text{FA}_{75}$, where bridgmanite/ LN -type phase coexists with corundum and hematite (see compositions in Table 3). This content is much higher than the maximum Al_2O_3 content in bridgmanite so far achieved, namely, 30 mol% at

Table 3Composition of Other Phases Coexisting With Bridgmanite and LiNbO_3 -Type Phase

Lett.	Phases	MgO	Al_2O_3	FeO	SiO_2	Total	Mg	Al	Fe^{3+}	Si	O
IRIS461											
En ₂₅ FA ₇₅	Cor (<i>n</i> = 10)	2.27 (11)	82.58 (40)	10.90 (62)	3.19 (13)	98.94 (91)	0.060 (3)	1.725 (9)	0.159 (8)	0.056 (2)	2.998 (1)
	Hem (<i>n</i> = 3)	6.25 (20)	7.12 (13)	80.14 (64)	0.35 (6)	88.93 (71)	0.219 (7)	0.197 (4)	1.575 (8)	0.008 (1)	2.895 (3)
FA ₁₀₀	Cor (<i>n</i> = 10)	83.63 (81)	14.57 (69)			97.93 (92)		1.604 (15)	0.396 (15)		3.000 (0)
	Hem (<i>n</i> = 11)	4.83 (41)	84.64 (84)			89.47 (71)		0.077 (7)	1.923 (7)		3.000 (0)
	Ox (<i>n</i> = 8)	26.82 (53)	63.15 (70)			89.96 (72)					
FA ₁₀₀	Cor (<i>n</i> = 10)	83.63 (81)	14.57 (69)			97.93 (92)		1.604 (15)	0.396 (15)		3.000 (0)
	Hem (<i>n</i> = 11)	4.83 (41)	84.64 (84)			89.47 (71)		0.077 (7)	1.923 (7)		3.000 (0)
	Ox (<i>n</i> = 8)	26.82 (53)	63.15 (70)			89.96 (72)					
IRIS493											
En ₂₅ FA ₇₅ + ⁵⁷ Fe ₂ O ₃	Cor (<i>n</i> = 10)	1.75 (11)	77.02 (78)	16.70 (24)	2.32 (20)	97.80 (91)	0.048 (3)	1.659 (5)	0.251 (5)	0.039 (3)	2.990 (1)
	Hem (<i>n</i> = 12)	6.27 (18)	7.20 (17)	79.61 (81)	0.36 (5)	93.43 (71)	0.223 (6)	0.203 (5)	1.565 (9)	0.006 (1)	2.887 (3)

Note. The total cation number of corundum and hematite is normalized to 2 assuming that all iron is ferric iron.

Abbreviations: Cor = Corundum; Hem = hematite; *n* = number of analysis points; Ox = iron oxide; Lett=Letter.

52 GPa and 2000 K (Liu et al., 2016; Liu, Nishi, et al., 2017). Furthermore, the present high FeAlO_3 content was obtained at 27 GPa, which is much lower than 52 GPa. The easier accommodation of the FeAlO_3 component compared to the Al_2O_3 component can be explained by the more similar ionic radii between Mg and Fe^{3+} compared to Mg and Al^{3+} as discussed above.

Nishio-Hamane et al. (2005) reported that the amount of the FeAlO_3 component in bridgmanite at pressures of 24 and 51 GPa was slightly lower and higher, respectively, than 25 mol% at 2100 K based on the laser-heated diamond anvil cell experiments. However, the present study demonstrates that the maximum solubility of the FeAlO_3 component in bridgmanite is much higher (65 mol%). This difference may be attributed to the challenge for LH-DAC experiments to achieve chemical equilibrium and also that FeAlO_3 -rich starting compositions were not used. Furthermore, Mössbauer spectroscopy demonstrates that some fraction of Fe^{3+} in starting materials are reduced under high-pressure and high-temperature conditions; hence, the assumption that Fe maintains its valence state throughout is not valid. We suggest that experiments using high-pressure multi-anvil technology provide more reliable information regarding equilibrium compositions compared to LH-DAC experiments.

4.4. Relations Between $\text{Fe}^{3+}/\Sigma\text{Fe}$ and Al^{3+} in Bridgmanite

Previous data suggest that the $\text{Fe}^{3+}/\Sigma\text{Fe}$ ratio in bridgmanite increases with increasing Al^{3+} content in bridgmanite at oxygen fugacities imposed by Fe and Re capsules at 24–26 GPa and 1900–2300 K (grey shaded region in Figure 5; McCammon, 1997; Lauterbach et al., 2000; Frost & Langenhorst, 2002; Saikia et al., 2009). In contrast, Hummer and Fei (2012) reported 100% $\text{Fe}^{3+}/\Sigma\text{Fe}$ in Al-free bridgmanite synthesized in the Pt capsule material at 25 GPa and 2000–2100 K, and Boffa Ballaran et al. (2012) obtained 93% $\text{Fe}^{3+}/\Sigma\text{Fe}$ -bearing bridgmanite with Al content of 0.36 PFU at 25 GPa and 1600 K under a hydrous environment. Our results at 27 GPa and 2000 K show that Al content has a limited effect on $\text{Fe}^{3+}/\Sigma\text{Fe}$ in bridgmanite (red-shaded region in Figure 5) when oxygen fugacity is high when Pt capsules are used for synthesis experiments. We note that the correlation between Fe^{3+} and Al^{3+} also depends on synthesis pressure and temperature, which will be discussed below. As mentioned above, however, the similar ionic radii of Al^{3+} and Si^{4+} promote substitution of Al^{3+} in the B site, which stabilizes Fe^{3+} in the A site even under reducing conditions to maintain charge balance. On other hand, oxidizing conditions stabilize Fe^{3+} , so that the Fe^{3+} content is independent of Al^{3+} content. Although it is possible that part of Fe^{3+} might be reduced to Fe^{2+} by charge-coupled substitution with Si^{4+} , there is no evidence for this possibility.

4.5. Partial Molar Volume of Bridgmanite

The molar volume of FeAlO_3 , AlAlO_3 , and FeSiO_3 -bearing bridgmanite is shown in Figure 6a, and lattice parameters are given in Table 4. Our data for FeAlO_3 -bearing bridgmanite agree with earlier data reported by Saikia et al. (2009) and Boffa Ballaran et al. (2012). To compare the effect of FeAlO_3 , AlAlO_3 , and FeSiO_3

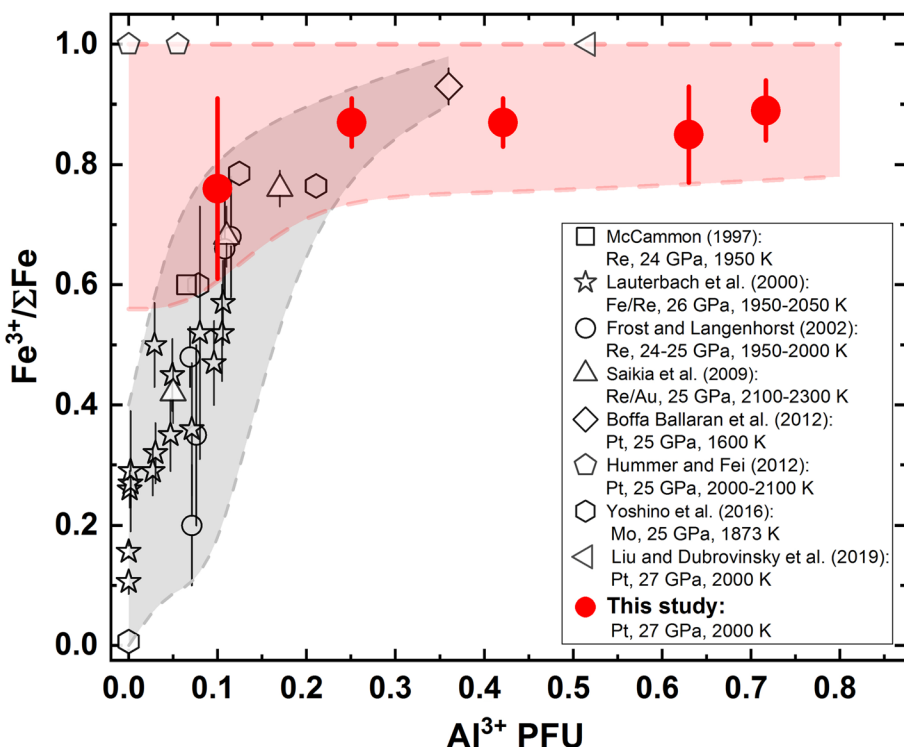


Figure 5. $\text{Fe}^{3+}/\Sigma\text{Fe}$ ratio of bridgmanite/LN-type phase as a function of its Al^{3+} content (PFU = atoms per formula unit with total cation number of two). Grey- and red-shaded regions represent estimated uncertainties of previous and present data, respectively.

components on the molar volume of bridgmanite, we fitted the current reported data using a linear function with molar volume of MgSiO_3 bridgmanite fixed to $24.44 \text{ cm}^3/\text{mol}$ (Horiuchi et al., 1987):

$$V(X) = 24.44 + (dV/dX) \times X_{\text{FeAlO}_3/\text{AlAlO}_3/\text{FeSiO}_3}, \quad (1)$$

where V is the molar volume in cm^3/mol and $X_{\text{FeAlO}_3/\text{AlAlO}_3/\text{FeSiO}_3}$ is the FeAlO_3 or AlAlO_3 or FeSiO_3 content in mol% in bridgmanite. Because the fractions of the $\text{MgAlO}_{2.5}$, $\text{MgFeO}_{2.5}$, and $\text{Fe}_{2/3}\text{SiO}_3$ components are limited in the present samples, we only consider the molar volumes of the FeAlO_3 , AlAlO_3 , and FeSiO_3 components in our calculation. Literature data (Mao et al., 1991; Andrault et al., 2001; Lundin et al., 2008; Tange et al., 2009; Dorfman et al., 2013; Wolf et al., 2015; Irfune et al., 1996; Zhang & Weidner, 1999; Daniel et al., 2004; Yagi et al., 2004; Walter et al., 2004, 2006; Liu et al., 2016; Liu, Nishi, et al., 2017) suggest that dV/dX for the FeSiO_3 and AlAlO_3 components are 0.0094 ± 0.0003 and $0.0140 \pm 0.0003 \text{ cm}^3/\text{mol}^2$, respectively, leading to partial molar volumes of 25.38 ± 0.03 and $25.84 \pm 0.03 \text{ cm}^3/\text{mol}$. We have subtracted the effects of the FeSiO_3 and AlAlO_3 components from the present volume data to derive the partial molar volume of the pure FeAlO_3 component. Following this process, we obtained the molar volume of $\text{MgSiO}_3\text{-FeAlO}_3$ bridgmanite as:

$$V(X) = 24.44 + 0.035 (1) \times X_{\text{FeAlO}_3} (0 < X_{\text{FeAlO}_3} \leq 36), \quad (2)$$

where the number in parentheses is the standard deviation of the last digit. We derived the partial molar volume of the FeAlO_3 component to be $27.9 \pm 0.1 \text{ cm}^3/\text{mol}$, which is much larger than the value for the other three components.

Figure 6b shows the molar volume of the LN-type phase as a function of the FeAlO_3 component fitted to the following equation:

$$V(X) = 24.89 (15) + 0.041 (3) \times X_{\text{FeAlO}_3} (36 < X_{\text{FeAlO}_3} < 70). \quad (3)$$

Comparison of equations (2) and (3) indicates that the volume of LN-type phase is larger than that of bridgmanite, which is expected since the LN-type phase forms on decompression to ambient pressure. The larger

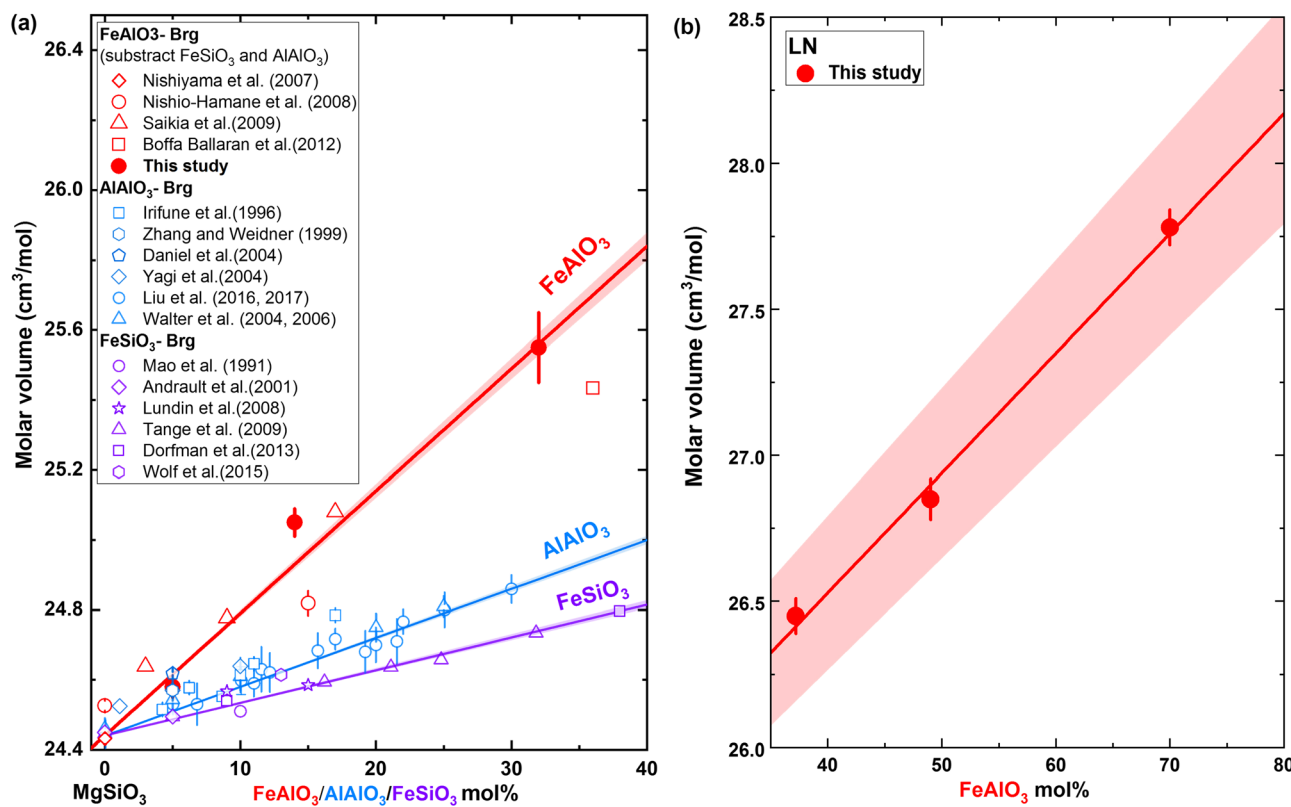


Figure 6. Molar volume of (a) FeAlO₃-, AlAlO₃-, and FeSiO₃-bearing bridgmanite and (b) LN-type phase in present and previous studies. The solid line shows the linear fitting results, while the shaded region indicates uncertainties of linear fitting. Brg = bridgmanite; LN = LiNbO₃-type phase.

dV/dX value for the LN-type phase compared to bridgmanite suggests that the transition of bridgmanite to the LN-type phase has a larger driving force at higher FeAlO₃ content, in agreement with our experimental observations.

Davies and Navrotsky (1983) and Navrotsky (1987) suggested that non-ideality of solid solutions is due to a mismatch of component volumes. Based on this idea, they expressed the Margules parameter of regular solutions (W_G in kJ/mol) by the following formula:

$$W_G = 100.8 \cdot \Delta V - 0.4 \frac{\text{kJ}}{\text{mol}}, \quad (4)$$

$$\Delta V = \frac{V_A - V_B}{(V_A + V_B)/2}, \quad (5)$$

Table 4
Lattice Parameters of Bridgmanite and LiNbO₃-Type Phase

Run No.	Starting composition	a (Å)	b (Å)	c (Å)	V (Å ³)	Molar V (cm ³ /mol)
Brg						
IRIS483	En ₉₀ FA ₁₀	4.792 (3)	4.950 (5)	6.934 (5)	164.55 (31)	24.77 (6)
IRIS428	En ₇₅ FA ₂₅	4.800 (2)	4.975 (4)	6.992 (5)	166.95 (37)	25.12 (4)
IRIS517	En ₆₀ FA ₄₀	4.799 (8)	5.022 (8)	7.072 (4)	170.45 (51)	25.65 (6)
LN						
IRIS517	En ₆₀ FA ₄₀	4.867 (3)	—	12.848 (13)	263.55 (63)	26.45 (6)
IRIS427	En ₅₀ FA ₅₀	4.886 (3)	—	12.936 (13)	267.51 (62)	26.84 (6)
IRIS461	En ₂₅ FA ₇₅	4.934 (3)	—	13.136 (9)	276.96 (45)	27.80 (5)

Abbreviations: Brg = bridgmanite; LN = LiNbO₃-type phase; V = volume.

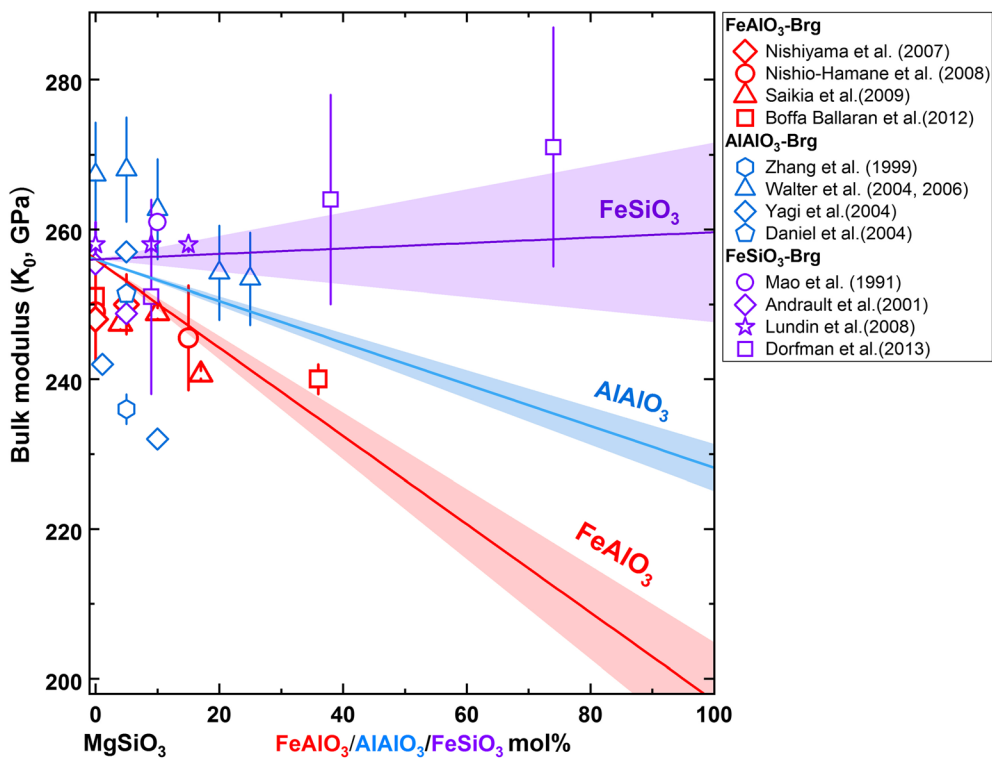


Figure 7. Bulk modulus of FeAlO₃-, AlAlO₃-, and FeSiO₃-bearing bridgmanite. Solid lines show linear fits, while shaded regions indicate uncertainties of linear fitting. The blue line and its uncertainty are derived from the theoretical study by Panero et al. (2006). Brg = bridgmanite.

where V_A and V_B are the molar volumes of the larger and smaller components, respectively. In the present case, the molar volumes of MgSiO₃, FeAlO₃, AlAlO₃, and FeSiO₃ components are 24.44, 27.94 ± 0.10 , 25.84 ± 0.03 and 25.38 ± 0.03 cm³/mol, respectively. These values give Margules interaction parameters of MgSiO₃-FeAlO₃, MgSiO₃-Al₂O₃ (i.e., AlAlO₃), and MgSiO₃-FeSiO₃ solid solutions as 13.1 ± 0.3 , 5.2 ± 0.1 , and 3.4 ± 0.1 kJ/mol, respectively. Thus, non-ideality of the FeAlO₃ component is much larger than for the AlAlO₃ and FeSiO₃ components. The maximum Al₂O₃ and FeSiO₃ contents reported so far are small, only 30 mol% (Liu et al., 2016; Liu, Nishi, et al., 2017) and 32 mol% (Tange et al., 2009), respectively. One may consider that solid solutions in MgSiO₃-Al₂O₃ and MgSiO₃-FeSiO₃ bridgmanite are limited due to non-ideality. However, our results suggest that the non-ideality of these solid solutions is much smaller than that of MgSiO₃-FeAlO₃ bridgmanite, and its compositional range extends to at least 67 mol% FeAlO₃. We suggest that Al₂O₃ and FeSiO₃ component amounts higher than 70 mol% should be possible in bridgmanite at higher pressures and temperatures.

4.6. Elasticity of Bridgmanite

Figure 7 shows the bulk modulus (K_0 , GPa) as a function of FeAlO₃, AlAlO₃, and FeSiO₃ components. We selected the value $K_0 = 256$ GPa for end-member MgSiO₃ bridgmanite determined at mid-lower mantle conditions by recent studies (Boffa Ballaran et al., 2012; Katsura et al., 2009; Tange et al., 2012). We then used a linear fit to evaluate the compositional effect on K_0 :

$$K_0 (X) = 256 + (dK_0/dX) \times X_{\text{FeAlO}_3/\text{AlAlO}_3/\text{FeSiO}_3}, \quad (6)$$

where $X_{\text{FeAlO}_3/\text{AlAlO}_3/\text{FeSiO}_3}$ is the FeAlO₃ or AlAlO₃ or FeSiO₃ content in mol% in bridgmanite. The value of dK_0/dX for FeAlO₃-bearing bridgmanite is derived to be -0.59 ± 0.08 GPa/mol using current data (Nishiyama et al., 2007; Nishio-Hamane et al., 2008; Saikia et al., 2009; Boffa Ballaran et al., 2012). Based on the large uncertainties of K_0 for FeSiO₃-bridgmanite reported by Dorfman et al. (2013), the derived dK_0/dX for the FeSiO₃ component is close to zero ($dK_0/dX = 0.03 \pm 0.12$ GPa/mol). Although there are many

studies on K_0 of AlAlO₃-bridgmanite (e.g., Zhang et al., 1999; Daniel et al., 2004; Yagi, et al., 2004; Walter et al., 2004, 2006), the reported data are highly scattered due to the strong variation of AlAlO₃ and MgAlO_{2.5} components with pressure (Brodholt, 2000; Liu, Ishii, & Katsura, 2017), temperature (Brodholt, 2000; Liu, Akaogi, & Katsura, 2019), and Mg/Si ratio of the bulk composition (Andrault et al., 2001; Liu, Boffa Ballaran, et al., 2019) in the lower mantle. We therefore used $dK_0/dX = -0.010 \pm 0.003$ GPa/mol for the AlAlO₃ component based on a theoretical study by Panero et al. (2006). The derived bulk modulus of hypothetical FeAlO₃ bridgmanite is 197 ± 8 GPa, which is significantly lower than that of FeSiO₃ (259 ± 12 GPa) and AlAlO₃ (255 GPa). The lower value suggests that a lower mantle dominated by FeAlO₃-bridgmanite would be more compressible than if it were dominated by FeSiO₃ or AlAlO₃-bridgmanite.

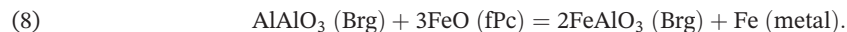
We derived the bulk sound velocity (V_ϕ) at ambient conditions based on estimated densities (ρ) and bulk moduli (K_0) of the three components for bridgmanite using the following equation:

$$V_\phi = \sqrt{\phi} = \sqrt{K_0/\rho}. \quad (7)$$

The derived values of V_ϕ for FeAlO₃, AlAlO₃, and FeSiO₃ bridgmanite are 7.9 ± 0.3 , 9.8 ± 0.1 , and 8.6 ± 0.4 km/s, respectively. The FeAlO₃ component thus gives lower velocities than the AlAlO₃ and FeSiO₃ components, hence has a large effect on the elasticity of bridgmanite.

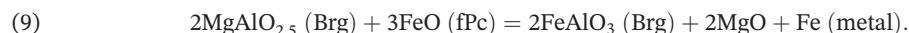
4.7. Expected Pressure Dependence of FeAlO₃ Solubility in Bridgmanite

Frost et al. (2004) proposed that bridgmanite coexists with ferropericlase and metallic iron in the lower mantle, so the incorporation of the FeAlO₃ component can be considered to occur by consumption of the AlAlO₃ component according to the following reaction:



Based on ambient conditions molar volumes of AlAlO₃, FeO, FeAlO₃, and Fe of 25.84, 12.06, 27.94, and 7.09 cm³/mol, respectively, the molar volume change for reaction (8) is found to be 0.95 cm³/mol. Therefore, we expect the maximum solubility of the FeAlO₃ component in bridgmanite to decrease with increasing pressure, which is consistent with the recent LH-DAC study by synchrotron Mössbauer spectroscopy (Shim et al., 2017) but inconsistent with discussion in Frost and McCammon (2008). Further studies of iron oxidation state in Fe- and Al-bearing bridgmanite at deep lower mantle conditions are required.

Significant amounts of the oxygen vacancy component MgAlO_{2.5} have been proposed for bridgmanite in the uppermost part of the lower mantle (Brodholt, 2000; Grüninger et al., 2019; Liu, Akaogi, & Katsura, 2019; Liu, Boffa Ballaran, et al., 2019; Liu, Ishii, & Katsura, 2017). Therefore, we also consider the incorporation of FeAlO₃ by consumption of MgAlO_{2.5} as follows:



The molar volumes of MgO and the MgAlO_{2.5} component in bridgmanite are 11.24 and 26.64 cm³/mol, respectively (Liu, Akaogi, & Katsura, 2019), so the molar volume change for reaction (9) is -4.0 cm³/mol. Therefore, we expect the amount of the MgAlO_{2.5} component to decrease with increasing pressure in order to form the FeAlO₃ component, whose amount is expected to increase with increasing pressure. The rapid decrease in the amount of the MgAlO_{2.5} component observed with increasing pressure in the MgSiO₃-MgAlO_{2.5} system (Liu, Akaogi, & Katsura, 2019) is thus strengthened by the presence of the FeAlO₃ component.

4.8. Implications for the Mineralogy of the Lower Mantle

We consider the amount of the FeAlO₃ component in uppermost lower mantle bridgmanite, namely, at conditions of 27 GPa and 2000 K. In a pyrolitic composition (Sun, 1982), the Si:Al:Fe:Mg ratio is 0.50:0.06:0.04:0.40. If bridgmanite is composed of MgSiO₃, FeSiO₃, and FeAlO₃ components and all excess MgO forms periclase, the ratio MgSiO₃:FeSiO₃:FeAlO₃ will be 0.85:0.06:0.09. Thus, the abundance of the FeAlO₃ component in bridgmanite in bulk pyrolitic mantle is far below its solubility limit. In a MORB composition (Green et al., 1979), the Si:Al:Fe:Mg ratio is 0.55: 0.21:0.07:0.17. If bridgmanite is composed of

MgSiO_3 , FeAlO_3 , and AlAlO_3 components and excess SiO_2 forms stishovite, their proportions will be 0.548:0.226:0.226. However, the solubility of the AlAlO_3 component in bridgmanite is only 12 mol% at 27 GPa and 2000 K, so the ratio of MgSiO_3 , FeAlO_3 , and AlAlO_3 components would change to 0.62:0.26:0.12. The amount of the FeAlO_3 component is still far below its maximum solubility in bridgmanite in the present study but outside the solubility limit reported by Nishio-Hamane et al. (2005; 24 mol%). Nevertheless, bridgmanite is the main phase for the FeAlO_3 component in the lower mantle.

Chemical heterogeneity is considered one possibility to explain seismically observed lateral velocity heterogeneities and slab stagnation in the middle lower mantle (e.g., Fukao & Obayashi, 2013; Karato & Karki, 2001; Kennett et al., 1998). Since bridgmanite is the most abundant phase in this region, knowledge of its chemistry is crucial for understanding seismically observed anomalies. The content of FeAlO_3 in bridgmanite changes from 9 to 22 mol% in going from bulk pyrolytic mantle to basaltic slabs. Furthermore, a decrease in $\Sigma\text{Fe}^{3+}/\text{Fe}$ ratio and oxygen vacancy component in bridgmanite has been proposed to explain slab stagnation in the mid-lower mantle (Liu, Ishii, & Katsura, 2017; Shim et al., 2017). Although the presence of the FeAlO_3 component may decrease with increasing depth based on the molar volume change for reaction (8), it should also suppress the oxygen vacancy component in bridgmanite. Furthermore, the dominant FeAlO_3 component may stabilize a dry bridgmanite because the charge-coupled component cannot provide cation sites to stabilize water in the crystal structure (e.g., Bolfan-Casanova et al., 2003; Litasov et al., 2003; Liu, Ishii, & Katsura, 2017; Navrotsky, 1999). These considerations suggest that subducted basaltic slabs dominated by bridgmanite may become stiffer than the bulk lower mantle. The variation of the FeAlO_3 component in bridgmanite may thus provide insight into seismically observed slab stagnation in the mid-lower mantle.

Acknowledgments

The authors thank E. Posner, H. Fei, D. Krause, R. Huang, R. Njul, H. Fischer, and S. Übelhack for assistance with sample and high-pressure assembly preparation. The manuscript was greatly improved by the constructive comments of two anonymous reviewers and the handling editor Stephen Parman. The synchrotron XRD measurements were carried out at beam line BL04B1 at SPring-8 (Proposal No. 2017B1078). All data used to produce the figures in this paper are available on Zendo (<http://doi.org/10.5281/zenodo.3378342>). Z. L. was financially supported by the Bayerisches Geoinstitut Visitor's Programme, the National Natural Science Foundation of China (41902034), and the Fundamental Research Funds for the Central Universities of Ministry of Education of China (Grant 45119031C037). This project received funding from the European Research Council (ERC) under the European Union's Horizon 2020 research and innovation program (Horizon 2020 Framework Programme; Proposal No. 787 527). It was also supported by research grants to T. K. (Bundesministerium für Bildung und Forschung [BMBF]: 05K13WC2 and 05K16WC2; Deutsche Forschungsgemeinschaft [DFG]: KA3434/3-1, KA3434/7-1, KA3434/8-1, and KA3434/9-1), L. D. (DU393/9-2 and DU393/13-1), and C. M. (MC3/20-2). All authors confirm no conflicts of interest and participated in discussion of results and preparation of the manuscript.

References

- Andrault, D., Bolfan-Casanova, N., Bouhifd, M. A., Guignot, N., & Kawamoto, T. (2007). The role of Al-defects on the equation of state of $\text{Al}-(\text{Mg},\text{Fe})\text{SiO}_3$ perovskite. *Earth and Planetary Science Letters*, 263, 167–179.
- Andrault, D., Bolfan-Casanova, N., & Guignot, N. (2001). Equation of state of lower mantle $(\text{Al},\text{Fe})\text{-MgSiO}_3$ perovskite. *Earth and Planetary Science Letters*, 193, 501–508.
- Andrault, D., Muñoz, M., Pesce, G., Cerantola, V., Chumakov, A., Kantor, I., et al. (2018). Large oxygen excess in the primitive mantle could be the source of the Great Oxygenation Event. *Geochemical Perspectives Letters*, 6, 5–10.
- Badro, J., Rueff, J. P., Vanko, G., Monaco, G., Fiquet, G., & Guyot, F. (2004). Electronic transitions in perovskite: Possible nonconvecting layers in the lower mantle. *Science*, 305(5682), 383–386. <https://doi.org/10.1126/science.1098840>
- Boffa Ballaran, T., Kurnosov, A., Glazyrin, K., Frost, D. J., Merlini, M., Hanfland, M., & Caracas, R. (2012). Effect of chemistry on the compressibility of silicate perovskite in the lower mantle. *Earth and Planetary Science Letters*, 333–334, 181–190.
- Bolfan-Casanova, N., Keppler, H., & Rubie, D. C. (2003). Water partitioning at 660 km depth and evidence for very low water solubility in magnesium silicate perovskite. *Geophysical Research Letters*, 30(17), 1905. <https://doi.org/10.1029/2003GL017182>
- Brodholt, J. P. (2000). Pressure-induced changes in the compression mechanism of aluminous perovskite in the Earth's mantle. *Nature*, 407(6804), 620–622. <https://doi.org/10.1038/35036565>
- Daniel, I., Bass, J. D., Fiquet, G., Cardon, H., Zhang, J., & Hanfland, M. (2004). Effect of aluminum on the compressibility of silicate perovskite. *Geophysical Research Letters*, 31, L15608. <https://doi.org/10.1029/2004GL020213>
- Davies, P. K., & Navrotsky, A. (1983). Quantitative correlations of deviations from ideality in binary and pseudobinary solid solutions. *Journal of Solid State Chemistry*, 46(1), 1–22. [https://doi.org/10.1016/0022-4596\(83\)90122-6](https://doi.org/10.1016/0022-4596(83)90122-6)
- Dorfman, S. M., Meng, Y., Prakpenka, V. B., & Duffy, T. S. (2013). Effects of Fe-enrichment on the equation of state and stability of $(\text{Mg},\text{Fe})\text{SiO}_3$ perovskite. *Earth and Planetary Science Letters*, 361, 249–257.
- Frost, D. J., & Langenhorst, F. (2002). The effect of $\text{AlO}_{1.5}$ on Fe-Mg partitioning between magnesiowüstite and magnesium silicate perovskite. *Earth and Planetary Science Letters*, 199, 227–241.
- Frost, D. J., Liebske, C., Langenhorst, F., McCammon, C. A., Tronnes, R. G., & Rubie, D. C. (2004). Experimental evidence for the existence of iron-rich metal in the Earth's lower mantle. *Nature*, 428(6981), 409–412. <https://doi.org/10.1038/nature02413>
- Frost, D. J., & McCammon, C. A. (2008). The redox state of Earth's mantle. *Annual Review of Earth and Planetary Sciences*, 36, 389–420.
- Fujino, K., Nishio-Hamane, D., Seto, Y., Sata, N., Nagai, T., Shinmei, T., et al. (2012). Spin transition of ferric iron in Al-bearing Mg-perovskite up to 200 GPa and its implication for the lower mantle. *Earth and Planetary Science Letters*, 317–318, 407–412.
- Fukao, Y., & Obayashi, M. (2013). Subducted slabs stagnant above, penetrating through, and trapped below the 660 km discontinuity. *Journal of Geophysical Research: Solid Earth*, 118, 5920–5938. <https://doi.org/10.1002/2013JB010466>
- Funamori, N., Yagi, T., Miyajima, N., & Fujino, K. (1997). Transformation in garnet from orthorhombic perovskite to LiNbO_3 -type phase on release of pressure. *Science*, 275(5299), 513–515. <https://doi.org/10.1126/science.275.5299.513>
- Glazyrin, K., Boffa Ballaran, T., Frost, D., McCammon, C., Kantor, A., Merlini, M., et al. (2014). Magnesium silicate perovskite and effect of iron oxidation state on its bulk sound velocity at the conditions of the lower mantle. *Earth and Planetary Science Letters*, 393, 182–186.
- Green, D. H., Hibberson, W. O., & Jaques, A. L. (1979). Petrogenesis of mid-ocean ridge basalts. In M. W. McElhinny (Ed.), *The Earth: Its origin, structure and evolution*, (pp. 269–299). London: Academic Press.
- Grüninger, H., Liu, Z., Siegel, R., Boffa Ballaran, T., Katsura, T., Senker, J., & Frost, D. (2019). Oxygen vacancy ordering in aluminous bridgmanite in the Earth's lower mantle. *Geophysical Research Letters*, 46, 8731–8740. <https://doi.org/10.1029/2019GL083613>
- Horiuchi, H., Ito, E., & Weidner, D. J. (1987). Perovskite-type MgSiO_3 : Single-crystal X-ray diffraction study. *American Mineralogist*, 72, 357–360.

- Hummer, D., & Fei, Y. (2012). Synthesis and crystal chemistry of Fe^{3+} -bearing $(\text{Mg}, \text{Fe}^{3+})(\text{Si}, \text{Fe}^{3+})\text{O}_3$ perovskite. *American Mineralogist*, 97, 1915–1921.
- Irifune, T. (1994). Absence of an aluminous phase in the upper part of the Earth's lower mantle. *Nature*, 370 (6485), 131–133.
- Irifune, T., Koizumi, T., & Ando, J. (1996). An experimental study of the garnet-perovskite transformation in the system MgSiO_3 – $\text{Mg}_3\text{Al}_2\text{Si}_3\text{O}_12$. *Physics of the Earth and Planetary Interiors*, 96(2–3), 147–157. [https://doi.org/10.1016/0031-9201\(96\)03147-0](https://doi.org/10.1016/0031-9201(96)03147-0)
- Ishii, T., Sinmyo, R., Komabayashi, T., Boffa-Ballaran, T., Kawazoe, T., Miyajima, N., & Katsura, T. (2017). Synthesis and crystal structure of LiNbO_3 -type $\text{Mg}_3\text{Al}_2\text{Si}_3\text{O}_12$: A possible indicator of shock conditions of meteorites. *American Mineralogist*, 102(9), 1947–1952.
- Ishii, T., Shi, L., Huang, R., Tsujino, N., Druzhbin, D., Myhill, R., et al. (2016). Generation of pressure over 40 GPa using Kawai-type multi-anvil press with tungsten carbide anvils. *Review of Scientific Instruments*, 87(2), 024501–1–024501–6.
- Ismailova, L., Bykova, E., Bykov, M., Cerantola, V., McCammon, C., Boffa Ballaran, T., et al. (2016). Stability of Fe, Al-bearing bridgmanite in the lower mantle and synthesis of pure Fe-bridgmanite. *Science Advances*, 2, e1600427.
- Karato, S., & Karki, B. B. (2001). Origin of lateral variation of seismic wave velocities and density in the deep mantle. *Journal of Geophysical Research*, 106, 21,771–21,783.
- Katsura, T., Funakoshi, K., Kubo, A., Nishiyama, N., Tange, Y., Sueda, Y., et al. (2004). A large-volume high-pressure and high-temperature apparatus for in situ X-ray observation, 'SPEED-Mk.II'. *Physics of the Earth and Planetary Interiors*, 143–144, 497–506. <https://doi.org/10.1016/j.pepi.2003.07.025>
- Katsura, T., Yokoshi, S., Kawabe, K., Shatskiy, A., Manthilake, M. G. M., Zhai, S., et al. (2009). P-V-T relations of MgSiO_3 perovskite determined by in situ X-ray diffraction using a large-volume high-pressure apparatus. *Geophysical Research Letters*, 36, L01305. <https://doi.org/10.1029/2008GL035658>
- Kennett, B. L. N., Widjiantoro, S., & van der Hilst, R. D. (1998). Joint seismic tomography for bulk sound and shear wave speed in the Earth's mantle. *Journal of Geophysical Research*, 103–112, 469–493.
- Kurnosov, A., Marquardt, H., Frost, D. J., Ballaran, T. B., & Ziberna, L. (2017). Evidence for a Fe^{3+} -rich pyrolytic lower mantle from (Al,Fe)-bearing bridgmanite elasticity data. *Nature*, 543(7646), 543–546. <https://doi.org/10.1038/nature21390>
- Lauterbach, S., McCammon, C. A., van Aken, P., Langenhorst, F., & Seifert, F. (2000). Mössbauer and ELNES spectroscopy of (Mg,Fe)(Si,Al) O_3 perovskite: A highly oxidised component of the lower mantle. *Contributions to Mineralogy and Petrology*, 138, 17–26.
- Litasov, K., Ohtani, E., Langenhorst, F., Yurimoto, H., Kubo, T., & Kondo, T. (2003). Water solubility in Mg-perovskites and water storage capacity in the lower mantle. *Earth and Planetary Science Letters*, 211(1), 189–203.
- Liu, Z. D., Akaoji, M., & Katsura, T. (2019). Increase of the oxygen vacancy component in bridgmanite with temperature. *Earth and Planetary Science Letters*, 505, 141–151.
- Liu, Z. D., Boffa Ballaran, T., Rong, H., Frost, D. J., & Katsura, T. (2019). Strong correlation of oxygen vacancy in bridgmanite with Mg/Si ratios. *Earth and Planetary Science Letters*, 523, 115697. <https://doi.org/10.1016/j.epsl.2019.06.037>
- Liu, Z. D., Irifune, T., Nishi, M., Tange, Y., Arimoto, T., & Shinmei, T. (2016). Phase relations in the system MgSiO_3 – Al_2O_3 up to 52 GPa and 2000 K. *Physics of the Earth and Planetary Interiors*, 257, 18–27. <https://doi.org/10.1016/j.pepi.2016.05.006>
- Liu, Z. D., Ishii, T., & Katsura, T. (2017). Rapid decrease of $\text{MgAlO}_{2.5}$ component in bridgmanite with pressure. *Geochemical Perspectives Letters*, 5, 12–18.
- Liu, Z. D., Nishi, M., Ishii, T., Fei, H. Z., Miyajima, N., Boffa Ballaran, T., et al. (2017). Phase relations in the system MgSiO_3 – Al_2O_3 up to 2300 K at lower-mantle pressures. *Journal of Geophysical Research: Solid Earth*, 10, 7775–7788. <https://doi.org/10.1002/2017JB014579>
- Liu, Z. D., Dubrovinsky, L., McCammon, C., Ovsyannikov, S. V., Koemets, I., Chen, L., et al. (2019). A new $(\text{Mg}_{0.5}\text{Fe}^{3+}_{0.5})(\text{Si}_{0.5}\text{Al}^{3+}_{0.5})\text{O}_3$ LiNbO_3 -type phase synthesized at lower mantle conditions. *American Mineralogist*, 104(8), 1213–1216. <https://doi.org/10.2138/am-2019-7070>
- Lundin, S., Catalli, K., Santillan, J., Shim, S.-H., Prakapenka, V. B., Kunz, M., & Meng, Y. (2008). Effect of Fe on the equation of state of mantle silicate perovskite over 1 Mbar. *Physics of the Earth and Planetary Interiors*, 168, 97–102.
- McCammon, C. A. (1997). Perovskite as a possible sink for ferric iron in the lower mantle. *Nature*, 387, 694–696.
- McCammon, C. A., Lauterbach, S., Seifert, F., Langenhorst, F., & van Aken, P. A. (2004). Iron oxidation state in lower mantle mineral assemblages: I. Empirical relations derived from high-pressure experiments. *Earth and Planetary Science Letters*, 222, 435–449.
- McCammon, C. A. (1994). Mössbauer spectroscopy of quenched high-pressure phases: Investigating the Earth's interior. *Hyperfine Interactions*, 90(1), 89–105. <https://doi.org/10.1007/bf02069120>
- Megaw, H. D. (1968). A note on the structure of lithium niobate, LiNbO_3 . *Acta Crystallographica. Section A*, 24, 583–588.
- Miyajima, N., Fujino, K., Funamori, N., Kondo, T., & Yagi, T. (1999). Garnet-perovskite transformation under conditions of the Earth's lower mantle: An analytical transmission electron microscopy study. *Physics of the Earth and Planetary Interiors*, 116(1–4), 117–131.
- Mao, H. K., Hemley, R. J., Fei, Y., Shu, J. F., Chen, L. C., et al. (1991). Effect of pressure, temperature, and composition on lattice parameters and density of (Fe,Mg) SiO_3 -perovskites to 30 GPa. *Journal of Geophysical Research*, 96(B5), 8069. <https://doi.org/10.1029/91jb00176>
- Nagai, T., Hamane, D., Devi, P. S., Miyajima, N., Yagi, T., Yamanaka, T., & Fujino, K. (2005). A new polymorph of FeAlO_3 at high pressure. *The Journal of Physical Chemistry B*, 109, 18,226–18,229.
- Navrotsky, A. (1999). A lesson from ceramics. *Science*, 284, 1788–1789.
- Navrotsky, A. (1987). Models of crystalline solutions. *Reviews in Mineralogy and Geochemistry*, 17, 35–69.
- Nishio-Hamane, D., Nagai, T., Fujino, K., Seto, Y., & Takafuji, N. (2005). Fe^{3+} and Al solubilities in MgSiO_3 perovskite: Implication of the $\text{Fe}^{3+}\text{AlO}_3$ substitution in MgSiO_3 perovskite at the lower mantle condition. *Geophysical Research Letters*, 32, L16306. <https://doi.org/10.1029/2005GL023529>
- Nishio-Hamane, D., Seto, Y., Fujino, K., & Nagai, T. (2008). Effect of FeAlO_3 incorporation into MgSiO_3 on the bulk modulus of perovskite. *Physics of the Earth and Planetary Interiors*, 166(3–4), 219–225. <https://doi.org/10.1016/j.pepi.2008.01.002>
- Nishiyama, N., Yagi, T., Ono, S., Gotou, H., Harada, T., & Kikegawa, T. (2007). Effect of incorporation of iron and aluminum on the thermoelastic properties of magnesium silicate perovskite. *Physics and Chemistry of Minerals*, 34(3), 131–143.
- Panero, W. R., Akber-Knutson, S., & Stixrude, L. (2006). Al_2O_3 incorporation in MgSiO_3 perovskite and ilmenite. *Earth and Planetary Science Letters*, 252, 152–161.
- Prescher, C., McCammon, C., & Dubrovinsky, L. (2012). MossA—A program for analyzing energy-domain Mössbauer spectra from conventional and synchrotron sources. *Journal of Applied Crystallography*, 45, 329–331.
- Richmond, N. C., & Brodholt, J. P. (1998). Calculated role of aluminum in the incorporation of ferric iron into magnesium silicate perovskite. *American Mineralogist*, 83, 947–951.
- Saikia, A., Boffa Ballaran, T., & Frost, D. J. (2009). The effect of Fe and Al substitution on the compressibility of MgSiO_3 perovskite determined through single-crystal X-ray diffraction. *Physics of the Earth and Planetary Interiors*, 173, 153–161.

- Shannon, R. D. (1976). Revised effective ionic radii and systematic studies of interatomic distances in halides and chalcogenides. *Acta Crystallographica. Section A*, 32, 751–767.
- Shim, S.-H., Grocholski, B., Ye, Y., Alp, E. E., Xu, S., Morgan, D., et al. (2017). Stability of ferrous-iron-rich bridgemanite under reducing midmantle conditions. *Proceedings of the National Academy of Sciences of the United States of America*, 114(25), 6468–6473. <https://doi.org/10.1073/pnas.1614036114>
- Sun, S. (1982). Chemical composition and the origin of the Earth's primitive mantle. *Geochimica et Cosmochimica Acta*, 46, 179–192.
- Tange, T., Kuwayama, Y., Irfune, T., Funamori, K., & Ohishi, Y. (2012). P - V - T equation of state of $MgSiO_3$ perovskite based on the MgO pressure scale: A comprehensive reference for mineralogy of the lower mantle. *Journal of Geophysical Research*, 117, N06201. <https://doi.org/10.1029/2011JB008988>
- Tange, Y., Takahashi, E., Nishihara, Y., Funakoshi, K., & Sata, N. (2009). Phase relations in the system MgO - FeO - SiO_2 to 50 GPa and 2000°C: An application of experimental techniques using multianvil apparatus with sintered diamond anvils. *Journal of Geophysical Research*, 114, B02214. <https://doi.org/10.1029/2008JB005891>
- Tsuchiya, T. (2003). First-principles prediction of the P - V - T equation of state of gold and the 660-km discontinuity in Earth's mantle. *Journal of Geophysical Research*, 108(B10), 2462. <https://doi.org/10.1029/2003JB002446>
- Walter, M., Kubo, A., Yoshino, T., Brodholt, J., Koga, K. T., & Ohishi, Y. (2004). Phase relations and equation-of-state of aluminous Mg -silicate perovskite and implications for Earth's lower mantle. *Earth and Planetary Science Letters*, 222, 501–516.
- Walter, M., Tronnes, R. G., Armstrong, L. S., Lord, O., Caldwell, W. A., & Clark, A. M. (2006). Subsolidus phase relations and perovskite compressibility in the system MgO - $AlO_{1.5}$ - SiO_2 with implications for Earth's lower mantle. *Earth and Planetary Science Letters*, 248, 77–89.
- Wolf, A. S., Jackson, J. M., Dera, P., & Prakapenka, V. B. (2015). The thermal equation of state of $(Mg, Fe)SiO_3$ bridgemanite (perovskite) and implications for lower mantle structures. *Journal of Geophysical Research: Solid Earth*, 120(11), 7460–7489. <https://doi.org/10.1002/2015jb012108>
- Xu, Y., McCammon, C. A., & Poe, B. T. (1998). The effect of alumina on the electrical conductivity of silicate perovskite. *Science*, 282(5390), 922–924. <https://doi.org/10.1126/science.282.5390.922>
- Yagi, T., Okabe, K., Nishiyama, N., Kubo, A., & Kikegawa, T. (2004). Complicated effects of aluminum on the compressibility of silicate perovskite. *Physics of the Earth and Planetary Interiors*, 143–144, 81–91. <https://doi.org/10.1016/j.pepi.2003.07.020>
- Yoshino, T., Kamada, S., Chengcheng, Z., Ohtani, E., & Hirao, N. (2016). Electrical conductivity model of Al-bearing bridgemanite with implications for the electrical structure of the Earth's lower mantle. *Earth and Planetary Science Letters*, 434, 208–219.
- Zhang, J., & Weidner, D. J. (1999). Thermal equation of state of aluminum enriched silicate perovskite. *Science*, 284(5415), 782–784. <https://doi.org/10.1126/science.284.5415.782>